Development of a Porous Solid Model for the Direct Reduction of Iron Ore Pellets

Quentin Fradet,* Mohammed Liaket Ali, and Uwe Riedel

The direct reduction of iron ore pellets with syngas or hydrogen is a promising technology to reduce the CO_2 emissions of the iron and steel industry. The conversion rate of single iron ore pellets to iron is extensively investigated. In most of these studies, a shrinking core model is employed to reproduce the experimental observations. However, this model presents an inherent bias by assuming a sharp separation between a fully converted region and a fully unreacted one. Herein the present study, an improved porous solid model is proposed. This model solves the mass balances of the individual gas species and the solid ones assuming spherical symmetry. The governing equations, the main algorithm, and validation cases are presented. The present model also offers wide flexibility to incorporate complex phenomena such as porosity changes or carbon deposition. Furthermore, the proposed model is integrated into a computational fluid dynamics (CFD) environment. It is verified that identical input parameters yield almost identical results in both frameworks, opening the gate toward reliable CFD simulations of industrial-scale reactors.

1. Introduction

Decarbonizing the steel industry is of utmost importance to achieve the EU target on combatting climate change. At the moment, steel is mainly (57.6%[1] in 2020) produced through the so-called integrated blast furnace (BF)-basic oxygen furnace (BOF) route. The rest, 42.4%, is obtained via the electric arc furnace (EAF) route, also called scrap route. The efforts of the last 60 years have reduced the CO_2 emissions per ton of steel by about 50%.[2] However, no clear decreasing trends can be observed over the past 20 years. These carbon-intensive processes have reached their thermodynamics limits[3] and breakthrough technologies are necessary in the light of EU emission targets.

While carbon reduction can be achieved by enforcing the circular economy via the EAF route, the primary steelmaking route

Q. Fradet, M. L. Ali, U. Riedel
Institute of Low-Carbon Industrial Processes
German Aerospace Center (DLR)
Walther-Pauer-Straße 5, 03046 Cottbus, Germany
E-mail: quentin.fradet@dlr.de

The ORCID identification number(s) for the author(s) of this article can be found under https://doi.org/10.1002/srin.202200042.

must be preserved. New approaches to reduce the CO_2 emissions of BFs involve the injection of hydrogen[4] or the injection of syngas obtained from the dry reforming of methane in the cowper stoves.[5] In addition to improvement on the BF, the direct reduction (DR) offers a promising alternative. This conversion process is currently fed with syngas originating from the reforming of natural gas. But reducing gases obtained from various feedstocks are practically possible: syngas (from coal or biomass), coke oven gas, methane, or even pure hydrogen from electrolysis. If pure hydrogen is used, carbon dioxide mitigation could reach 95% with "green" electricity.[6] However, even with natural gas, the DR-EAF route reaches emissions well below 1 ton of CO_2 per ton of crude steel[2] against 1.3–1.8 tons for the conventional BF route.

This mitigation potential comes with an increase in the operating costs, in addition to investment costs.[7] Research, development, and innovation are needed to transition from pilot-phase to industrial-scale deployment. Computational fluid dynamics (CFD) simulations of DR shaft furnaces[8] can support the understanding of the process, help optimize and predict the process conditions, or can even be used for design purposes. However, the modeling of this multiphase reacting system has inherent complexities. In addition to an appropriate gas-phase chemistry modeling, there is a need for a realistic pellet conversion model. The model should cover any composition that can be found in the reactor, mainly syngas but also the reduction products, CO_2 and H_2O, or methane. Such DR shaft furnaces are also characterized by an inhomogeneous temperature distribution due to heat losses, exothermic and endothermic reactions.

Many experiments on single pellets using thermogravimetric analysis (TGA) have been conducted to derive a reduction model at a pellet level.[9–17] The output is the so-called conversion degree, which corresponds to the mass evolution of the pellet. This experimental output does not provide information on the solid's real state, such as the composition or the porosity. Therefore, even very simplified models, such as a one-interface shrinking core model, can give a satisfactory agreement when reproducing a single TGA result, but the derived parameters are valid for these specific conditions only. This lack of experimental constraints present in real system means that better models need to be proposed, anchored more firmly by the physics of transport in porous media.[18] Furthermore, new models must be generic enough to encompass all conditions encountered in CFD simulations of shaft reactors.

**ADVANCED
SCIENCE NEWS**

www.advancedsciencenews.com

**steel
research**
international

www.steel-research.de

In the present study, a modeling framework is proposed that should faithfully transcribe the solid state during the reduction and decouple the transport and reaction processes, thus offering a groundwork to develop reliable chemical mechanisms. This model solves the reduction process at the pellet level considering a spherical symmetry, that is, in one spatial dimension. Once developed, this model was transposed into a multidimensional CFD environment. Here, the whole domain of the experimental setup is included in the simulation and uses the kinetic data developed previously. Both models will be confronted to two experimental test cases from the literature, one using pure hydrogen and the second using a syngas mixture. We will see that the CFD model can retrospectively give input data for the 1D model: assumptions are needed for the boundary condition of the 1D model while it is solved in the CFD model. This additional information allows further to refine the kinetic rate data used in the model.

This paper is organized as follows: the theory behind the 1D model will be presented first; this includes the governing equations and their development toward solvable mathematical expressions. Then, the focus will be put on the integration of the model into a multiphase CFD environment. The experimental data chosen to support the models will then be introduced before going into Results and Discussion section.

2. Modeling Approaches

2.1. Porous Solid Model

The shrinking core model is traditionally used for describing the reduction of single hematite pellets.[19,20] It assumes an unreacted nonporous region and a fully converted region separated by a moving reaction front. The model gains accuracy when extended to the intermediate iron oxides, magnetite (Fe_3O_4), and wüstite (FeO),[21,22] but the inherent flaws of the approach remains. Also, the model output is a global source term that relies on a continuous description of the space. This brings challenges for its adaptation in a CFD environment, which is inherently discretized, usually with the finite volume method.

The present porous solid model does not rely on moving fronts but on the discretization of the pellet along the radius, assuming a spherical symmetry. As it will be further evoked, this 1D approach allows for a much smoother adaptation into the CFD multidimensional approach. This model was developed in Python, using Cantera[23] to handle the multiphase chemistry.

2.1.1. Governing Equations

The present model is based on governing equations of the gas and solid species, which are valid anywhere inside the porous solid pellet

$$\frac{\partial \varepsilon C_i}{\partial t} = -\nabla\cdot(-D^{\text{eff}}\nabla C_i) + \dot{s}_i, \quad i \in \text{ gas species} \tag{1}$$

$$\frac{\partial(1-\varepsilon)\rho_j X_j}{\partial t} = M_j \dot{s}_j, \quad j \in \text{solid species} \tag{2}$$

Here, and in the following, the index i will be used for an arbitrary gas-phase species and j for any solid species.

Equation (1) is the gas species concentration equation with diffusion and reaction. It can be derived from a continuity equation where the advection is neglected and where the first Fick's law is utilized. As the transport of the gaseous species occurs in a porous medium, noticeable changes are brought at the reaction–diffusion equation. The porosity ε is adjoined to the bulk concentration C_i to account that the gas only occupies the volume V_g in the total volume $V = V_g + V_s$. The diffusion coefficient also differs from the molecular bulk diffusion coefficient D. An effective diffusivity D^{eff} is used, where $D^{\text{eff}} = (\varepsilon/\tau)D$, and where τ is the tortuosity factor.[24]

Equation (2) is the solid species mole fraction equation with reaction. This equation is derived from a mass balance on individual solid species. ρ_j and X_j are respectively the density of the species j in a pure solid state and the mole fraction of the species j. The solid is assumed to be ideal, which means that the density of the solid is a linear combination of the species densities, $\rho_s = \sum_j \rho_j X_j$.

$\dot{s}_{i/j}$ appears in Equations 1 and 2, which is the net chemical production rate of the species i or j due to surface reactions. The molar weight M_j is added in Equation (2) for units' correspondence.

As mentioned earlier, ρ_j is a constant and can therefore be written outside of the derivative term of Equation (2). However, the term involving the porosity (ε) cannot be assumed constant. It was determined experimentally by Towhidi et al.[16] that the pellet porosity increases considerably during the reduction process. They measured an initial porosity of 15.8% and a porosity after reduction of about 61.0%. The PDE on the solid species can be decomposed into

$$X_j \frac{\partial(1-\varepsilon)}{\partial t} + (1-\varepsilon)\frac{\partial X_j}{\partial t} = \frac{M_j}{\rho_j}\dot{s}_j, \quad j \in \text{solid species} \tag{3}$$

This equation can be summed up over all solid species and after applying the sum rule for derivatives and using the property $\sum_j X_j = 1$, Equation (3) can be reduced to a partial differential equation on the porosity

$$\frac{\partial \varepsilon}{\partial t} = -\sum_j \frac{M_j}{\rho_j}\dot{s}_j, \quad j \in \text{solid species} \tag{4}$$

Expanding Equation (1) in a similar way as did for Equation (2) gives the Equation (5), in which the porosity dependence can be eliminated by Equation (4). We obtain a set of PDEs with time derivatives of the gas concentration and solid mass fraction solely (i.e., without the porosity term)

$$\frac{\partial C_i}{\partial t} = \frac{1}{\varepsilon}\nabla\cdot(D^{\text{eff}}\nabla C_i) + \frac{1}{\varepsilon}\dot{s}_i - \frac{C_i}{\varepsilon}\frac{\partial \varepsilon}{\partial t}, \quad i \in \text{gas species} \tag{5}$$

and

$$\frac{\partial X_j}{\partial t} = \frac{1}{1-\varepsilon}\frac{M_j}{\rho_j}\dot{s}_j + \frac{X_j}{1-\varepsilon}\frac{\partial \varepsilon}{\partial t}, \quad j \in \text{solid species} \tag{6}$$

The equations presented so far were valid in any coordinate. In this work, a spherical symmetry was assumed. Equation (5) can be written in spherical coordinates as

$$\frac{\partial C_i}{\partial t} = \frac{1}{\varepsilon}\frac{1}{r^2}\frac{\partial}{\partial r}\left(r^2 D^{\text{eff}}\frac{\partial C_i}{\partial r}\right) + \frac{1}{\varepsilon}\dot{s}_i - \frac{C_i}{\varepsilon}\frac{\partial \varepsilon}{\partial t}, \quad i \in \text{gas species} \tag{7}$$

with r being the radial coordinate.

2.1.2. Discretization

To solve the dependent variables (ε, C_i, X_j) of the PDEs (Equation (4)–(7)), the method of lines[25] is employed. The method reduces the time- and space-dependent PDEs into a system of ordinary differential equations (ODEs) by discretizing the spatial derivatives and leaving the time variable continuously. The radial dimension is discretized into a finite grid counting N points with a constant spacing Δr.

The discretization method presented in Versypt et al.[26] for the gas-phase species Equation (7) has been adopted here, as it showed stability and accuracy in handling cases where the diffusivity is a function of position. After applying this central finite difference scheme to the spatial derivative, it follows

$$\frac{dC_i^k}{dt} = \frac{1}{\varepsilon^k}\left[\frac{D^{\text{eff},k}}{2k\Delta r^2}((k+2)C_i^{k+1} - 2kC_i^k + (k-2)C_i^{k-1})\right.$$
$$\left. + \frac{D^{\text{eff},k+1}}{2\Delta r^2}(C_i^{k+1} - C_i^k) + \frac{D^{\text{eff},k-1}}{2\Delta r^2}(C_i^{k-1} - C_i^k)\right]$$
$$+ \frac{1}{\varepsilon^k}\dot{s}_i^k - \frac{C_i^k}{\varepsilon^k}\frac{d\varepsilon^k}{dt}, \quad i \in \text{gas species}, \quad k \in [1, N-1] \tag{8}$$

The discretization of the other PDEs, Equation (4) and (6), is straightforward as no spatial derivative is present

$$\frac{dX_j^k}{dt} = \frac{1}{1-\varepsilon^k}\frac{M_j^k}{\rho_j^k}\dot{s}_j^k + \frac{X_j^k}{1-\varepsilon^k}\frac{d\varepsilon^k}{dt}, \quad j \in \text{solid species} \tag{9}$$

and

$$\frac{d\varepsilon^k}{dt} = -\sum_j \frac{M_j^k}{\rho_j^k}\dot{s}_j^k, \quad j \in \text{solid species} \tag{10}$$

2.1.3. ODEs Solution and Conversion-Rate Calculation

Equation (8)–(10) can be written in the simplified form

$$\dot{\mathbf{y}} = \mathbf{f}(t, \mathbf{y}, \mathbf{c}) \tag{11}$$

where $\mathbf{y}$ represents the array of dependent variables, t represents the independent variable (i.e., the time), and $\mathbf{c}$ represents an array of constants. In detail, the dependent variables in the current system of equation are $\mathbf{y} = [C_{i=0}^{k=0}, \ldots, C_{i=0}^{k=N}, C_{i=1}^{k=0}, \ldots, C_{i=1}^{k=N}, \ldots, X_{j=0}^{k=0}, \ldots, X_{j=0}^{k=N}, \ldots, \varepsilon^{k=0}, \ldots, \varepsilon^{k=N}]$. Here, the SciPy function "solve_ivp" was chosen to solve this system of ordinary differential equations with a given initial state.

The effective diffusivity, D^{eff}, that appears in Equation (7) involves the bulk diffusion coefficient, which needs to be determined. Cantera has built-in tools to estimate binary diffusion coefficients. However, the capabilities of the CFD code for the transport properties are more limited as it can only calculate a mixture diffusion coefficient derived from the mixture viscosity. Thus, to achieve comparable results, the CFD transport models were transposed in the 1D model. The dynamic viscosity is first calculated using the following correlation

$$\mu = \frac{C_1 T^{C_2}}{1 + C_3/T + C_4/T^2} \tag{12}$$

The mixture viscosity is calculated with a mass fraction averaging. Then, the bulk diffusion is obtained by dividing with the Schmidt number and the gas density

$$D = \frac{\mu}{\rho_g \text{Sc}} \tag{13}$$

Equation (8) and (9) contain the local reaction source terms, $\dot{s}_{i/j}^k$. The open-source suite of tools Cantera[23] has been integrated in the model to solve for the chemical kinetic and transport calculations. Concerning the chemistry, each reaction was written as a first-order reaction regarding the gaseous species concentrations and the solid species mole fraction. For example, for the reaction

$$3\,\text{Fe}_2\text{O}_3 + \text{H}_2 \rightarrow 2\,\text{Fe}_3\text{O}_4 + \text{H}_2\text{O} \tag{14}$$

the chemical source term S is written

$$S = kC_{\text{H}_2}X_{\text{Fe}_2\text{O}_3} \tag{15}$$

In the end, the system of ODE that we solve, Equation (11), has unknown parameters of three kinds: i) one unknown parameter, τ, related to the intra-pellet transport. ii) Each reaction brings an unknown parameter, the rate constant k. The Arrhenius equation is usually employed to express the rate constant, but this would bring a pair of parameters, the pre-exponential factor A and the activation energy E_a, which cannot be independently solved under the present isothermal conditions. iii) Assumptions have to be made regarding the boundary conditions of the gas phase species. One possibility is to consider the incoming flux from the far field. This brings an additional unknown to the system, the external mass transfer coefficient. The method retained in this work is to first neglect the external mass transport limitations by assuming $C_i^N(t) = C_i^\infty$ for all i. Later, the results of the CFD simulations will provide accurate boundary conditions for this 1D model.

Once the system of equations has been solved, the conversion degree as a function of time can be retrieved from the solid species mole fractions. At a macroscopic level, the global conversion degree F is obtained via

$$F(t) = \frac{m_0 - m(t)}{m_0 - m_\infty} \tag{16}$$

where m_0, $m(t)$ and m_∞ are the initial mass of the pellet, the mass of the pellet at a time t, and its theoretical mass after complete reduction, respectively. To calculate this global conversion in the model, local conversions are determined through

$$\varphi(t) = \frac{\omega_0 - \omega(\mathbf{x}, t)}{\omega_0 - \omega_\infty} \tag{17}$$

with

$$\omega(\mathbf{x}, t) = (1 - \varepsilon(\mathbf{x}, t)) \sum_j \rho_j X_j(\mathbf{x}, t) \tag{18}$$

The local conversion degrees can finally be integrated to yield the global conversion

$$F(t) = \frac{\iiint_V \varphi(\mathbf{x}, t) \, \mathrm{d}V}{V} \tag{19}$$

2.2. CFD Model

For most applications, CFD relies on numerically solving the Navier–Stokes equations, that is, the continuity and momentum equations

$$\frac{\partial \rho}{\partial t} + \nabla \cdot (\rho \mathbf{v}) = 0 \tag{20}$$

$$\frac{\partial \rho \mathbf{v}}{\partial t} + \nabla \cdot (\rho \mathbf{v}\mathbf{v}) = \nabla \cdot \bar{\bar{\tau}} - \nabla p + \rho \mathbf{g} \tag{21}$$

In the last equations, p is the pressure, $\bar{\bar{\tau}}$ is the deviatoric stress tensor, and $\mathbf{g}$ the gravity vector. For a multicomponent phase, this set of equation can be completed by transport equations for the species mass fractions

$$\frac{\partial \rho Y_i}{\partial t} + \nabla \cdot (\rho Y \mathbf{v}) = -\nabla \cdot \mathbf{j}_i + \dot{\omega}_i \tag{22}$$

where Y_i, $\mathbf{j}_i$, and $\dot{\omega}_i$ are the local mass fraction, the diffusion flux, and the chemical source term, respectively, resulting from homogeneous reactions; all terms being evaluated for the species i. As the considered test cases are all isothermal, no energy equations are needed.

The CFD open source toolbox OpenFOAM[27] was used to develop an appropriate solver for the reduction of iron oxide pellets. To account for the gas–surface interactions (two-phase flow), the following modifications were made

$$\frac{\partial \alpha_g \rho_g}{\partial t} + \nabla \cdot (\rho_g \mathbf{v}_g) = S_g \tag{23}$$

$$\frac{\partial \alpha_g \rho_g \mathbf{v}_g}{\partial t} + \nabla \cdot (\rho_g \mathbf{v}_g \mathbf{v}_g) = \nabla \cdot \bar{\bar{\tau}} - \nabla p + \rho_g \mathbf{g} + \mathbf{M}_{sg} \tag{24}$$

$$\frac{\partial \alpha_g \rho_g Y_{g,i}}{\partial t} + \nabla \cdot (\rho_g Y_{g,i} \mathbf{v}_i) = -\nabla \cdot \mathbf{j}_{g,i}^{\mathrm{eff}} + M_i \dot{\omega}_i + M_i \dot{s}_i \tag{25}$$

These equations for the gas phase (continuity, momentum, and species transport) are accompanied by Equation (4) and (6) for the solid phase (porosity and species). In Equation (23)–(25), α_g is the gas volume fraction. It is mathematically equivalent to the porosity ($\alpha_g = V_g/(V_g + V_s)$), but used here for clarity, as it is also defined in the gas region ($\alpha_g = 1$).

This set of equations is valid over the whole domain, in the pellet region, and in other zones of the reactor. The viscous stress tensor is handled by the native solver for Newtonian fluids with

$\bar{\bar{\tau}} = \mu[\nabla \mathbf{v}_g + (\nabla \mathbf{v}_g)^T] - 2/3\mu(\nabla \times \mathbf{v}_g)\bar{\bar{\mathrm{I}}}$. Homogeneous chemistry among the gas species is taken into account through the term $\dot{\omega}_i$. No homogeneous reactions were considered in the present work.

In the pellet region, terms related to the gas/solid chemistry and to the gas transport in the solid are considered. $\dot{s}_i$, the chemical source term is solved by the native software option. The same reactions and the same reaction rates will be used in 1D model and in the CFD. There is a net mass transfer between both phases, given by $S_g = \sum_i M_i \dot{s}_i = -\sum_j M_j \dot{s}_j$. In Equation (24), $\mathbf{M}_{sg}$ is the momentum sink term for the flow through the porous medium. It was modeled here by Darcy's law, $\mathbf{M}_{sg} = -\mu_g \mathbf{D} \mathbf{v}_g$, where $\mathbf{D}$ is a constant coefficient. The effective diffusion flux $\mathbf{j}_{g,i}^{\mathrm{eff}}$ can be extended to $\mathbf{j}_{g,i}^{\mathrm{eff}} = -\rho_g D^{\mathrm{eff}} \nabla Y_{g,i}$. The same approach for D^{eff} was used in the CFD model as in the 1D model (see Equation (12) and (13)).

In the gas phase where there is no pellet, $\alpha_g = 1$ and we retrieve Equation (20)–(22). In this region, all interaction terms vanish (S_g, $\mathbf{M}_{sg}$, $\dot{s}_i$) and the diffusion flux is calculated with the bulk diffusion coefficient.

The global conversion is calculated in a similar manner to the 1D model. A local conversion can be calculated for each cell. Then, these terms are summed up and weighted by the individual cell volume over the total volume.

2.3. Supportive Experimental Data

The results and discussions will rely upon two data sets from the literature. The first case is a pellet reduced in pure hydrogen at 1123 K. The data set is taken from Kazemi et al.[17] In the second data set, the pellet reduction is achieved in a syngas atmosphere ($H_2/CO = 60/40\%$) also at 1123 K and the data are taken from Kazemi et al.[13] For simplicity, these two data sets will be denoted Case 1 and Case 2 in the remainder of this paper. Further information regarding these data sets are summed up in **Table 1**.

3. Results and Discussions

3.1. Validation and Results of the 1D Model

3.1.1. Validation of the Diffusion Discretization Scheme

A first verification of the implementation of the discretization of diffusion terms can be done following Versypt's method.[26] In

Table 1. Experimental data sets studied.

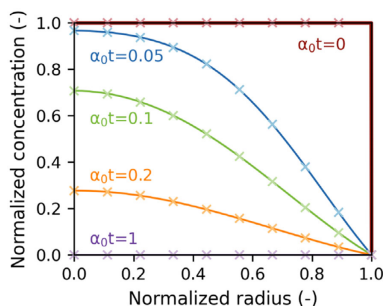| Test case name	Case 1	Case 2
Author	Kazemi et al. 2017[17]	Kazemi et al. 2014[13]
Gas composition [vol%]	H_2:100	H_2:60/CO:40
Gas flow rate [Nl min^{-1}]	2	1
Temperature [K]	1123	1123
Pressure [atm]	1	1
Pellet composition [wt%]	Fe_2O_3: 0.96/Gangue: 0.04	Fe_2O_3: 0.96/Gangue: 0.04
Pellet porosity [%]	26	27
Pellet diameter [mm]	11	11

Figure 1. Dimensionless concentration as a function of dimensionless position. The analytical solution is shown by solid curves while the numerical solution is shown with markers. The calculation was run on 30 points, but fewer points are shown for clarity.

this part, no chemistry is considered, and the attention is only drawn toward the spatial evolution of a binary gas system with given initial conditions and fixed boundary conditions. The verification is limited to a constant diffusivity case, where a simple analytical solution exists. At the initial time step, the concentration is 1 everywhere inside the solid, except at the surface, where the concentration is 0.

The concentration evolution for this validation case is shown in **Figure 1**. It can be seen that the discretization scheme proposed by Versypt perfectly matches the analytical solution. Versypt also has shown that his scheme is applicable to space- and time-dependent diffusivity.

3.1.2. Grid Convergence

The solver automatically set appropriate time steps; the number of spatial points can, in contrast, be freely set. This number of points should be high enough to reach the grid convergence. Simulation results are shown in **Figure 2** with a varying number of spatial points (5, 15, and 50). The calculations were run for the two cases previously presented in Table 1; details on the chemistry will be given in the next section. It can be seen that in both cases, the convergence is quickly achieved. The deviations observed between 5 and 15 points is small, and is negligible between 15 and 50 points. Therefore, in the remainder of the paper, all 1D calculations were run using 30 points.
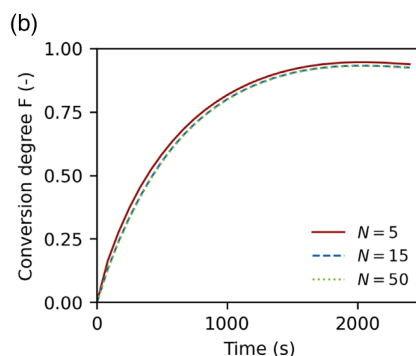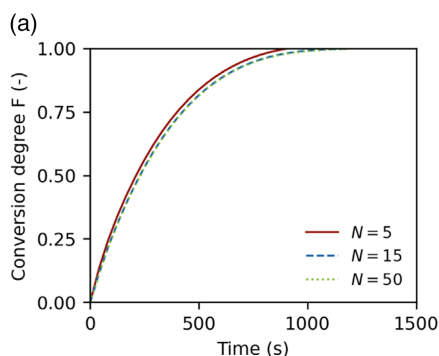
3.1.3. Details of Simulation Runs

As mentioned in Section 2.1.3, there are unknowns related to an intra-pellet property, τ, to the boundary conditions and to the chemistry. The tortuosity has been set throughout this paper and for both cases to 5.0, and the external transport limitations are initially neglected. The chemical parameters can be quickly optimized as the time for each run is only about 1 s. For Case 1, as only hydrogen is present, three reactions are sufficient for a complete description of the chemical process. The rate constant of each these reactions was fitted with this Case 1. The chemical mechanism is extended for Case 2 to the reduction with CO, which leads to three analogous reactions of the reduction of the oxides. Two additional reactions are included: the decomposition of CO into carbon and the formation of cementite from carbon and iron. The rate constants of these five additional reactions were fitted with Case 2. The value of the rate constants after this first round of optimization can be found in **Table 2**.

As it can be seen in **Figure 3**, the model is able to accurately reproduce the documented experimental data sets of Case 1 and Case 2. The temperature is similar in both cases, only the gas composition changes, from pure H_2 to $H_2/CO = 60/40$ vol%. It can be seen that the model can effectively retrieve the experimental observations, that is, the so-called conversion degree over time. This definition can be misleading, as it expresses the mass change of the sample rather than the conversion of the oxides into the metal. For example, the conversion degree in the syngas case does not reach 100%, not because of unconverted oxides, but because of the presence of carbon (in cementite or graphite form) that contributes to the pellet mass, and thus prevents it from increasing up to the theoretical mass after reduction.

In addition, the model can output the pellet and the gas states at any simulation time. As a matter of example, some points have been extracted from the simulation displayed in Figure 3 and further results at these states are displayed in the following figures.

Figure 4 corresponds to a pellet conversion of 50% with pure hydrogen (Case 1), which means at about 230 s of reduction time. Four graphs (a–d) have been plotted, which show the local conversion degree, the gas species concentrations, the solid mole fractions, and the porosity over the pellet radius. Figure 4a shows

Figure 2. Examples of calculation convergence with respect to the number of spatial points with a) Case 1 and b) Case 2. In both cases, three different numbers of points have been tested: 5, 15, and 50.

Table 2. The first set of chemical parameters obtained by assuming constant boundary conditions.

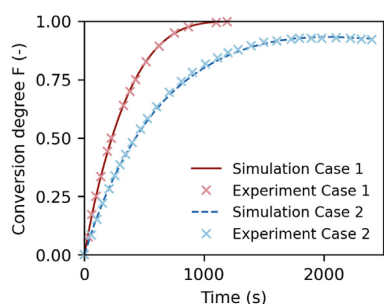| Reaction	Rate constant k
$3\,Fe_2O_3 + H_2 \rightarrow 2\,Fe_3O_4 + H_2O$	$48.7\ s^{-1}$
$Fe_3O_4 + H_2 \rightarrow 3\,FeO + H_2O$	$64.9\ s^{-1}$
$FeO + H_2 \rightarrow Fe + H_2O$	$24.5\ s^{-1}$
$3\,Fe_2O_3 + CO \rightarrow 2\,Fe_3O_4 + CO_2$	$18.9\ s^{-1}$
$Fe_3O_4 + CO \rightarrow 3\,FeO + CO_2$	$23.7\ s^{-1}$
$FeO + CO \rightarrow Fe + CO_2$	$9.5\ s^{-1}$
$2\,CO \rightarrow C + CO_2$	$0.24\ m^3\,mol^{-1}\,s^{-1}$
$3\,Fe + C \rightarrow Fe_3C$	$401\ mol\,m^{-3}\,s^{-1}$

Figure 3. Conversion degree over time of the reduction of iron ore for Case 1 (in red) and Case 2 (in blue). The markers are the experimental data from Kazemi et al.[13,17] and the lines are the results of the 1D model assuming constant boundary conditions.
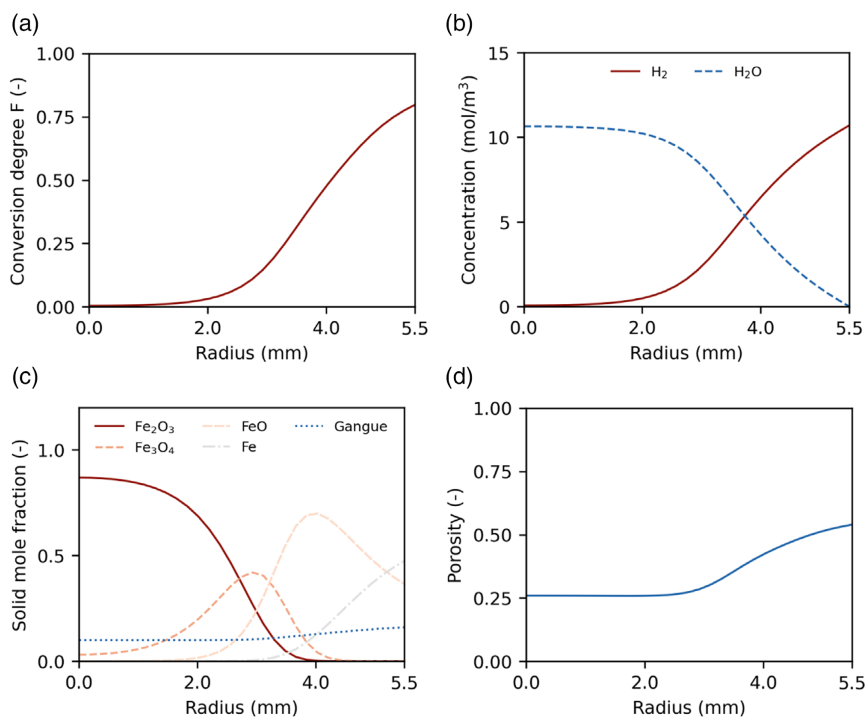
clearly an unreacted core while the surface reduction reaches about 80%. It is notable that Fe is mainly present only where Fe_2O_3 and Fe_3O_4 are already converted. From the Figure 4b,c, it is possible to identify neither a fully diffusion-controlled regime nor a fully reaction-controlled one. On the contrary, both processes participate in the resistance to the conversion. The porosity at the surface, visible in Figure 4d, is about 55%. This porosity corresponds to a reduction of 80%; after full reduction, its value reaches 61%, in agreement with the experimental observations of Towhidi.[16]

The results for the syngas case at 50% of reduction, **Figure 5**, show globally similar trends. For the same experimental temperature, the presence of 40% of CO increases the half reduction time to 434 s, which means about a factor two. Another difference lies in the presence of carbon, which has two forms, cementite and free carbon. The amount of carbon in the present case, Figure 5c, is small, but is subject to increase during the reduction process. Unlike the oxide reduction, the carbon deposition will decrease the porosity and may ultimately hinder the reduction process considerably. Another noticeable difference between the hydrogen and syngas case is the shape of the conversion over the radius. For the same global conversion, 50%, the syngas case tends to have a higher conversion near the surface (88% in the present case) and a lower one at the center. This may be due to the presence of CO that decreases the gas diffusion and thus shifts the reduction toward a diffusion-controlled regime.

Figure 6 shows the state of the pellet composition at the last time step of Case 1 (Figure 6a) and of Case 2 (Figure 6b). The pellet reduced with pure hydrogen shows almost constant final values, the conversion being slightly below 100%
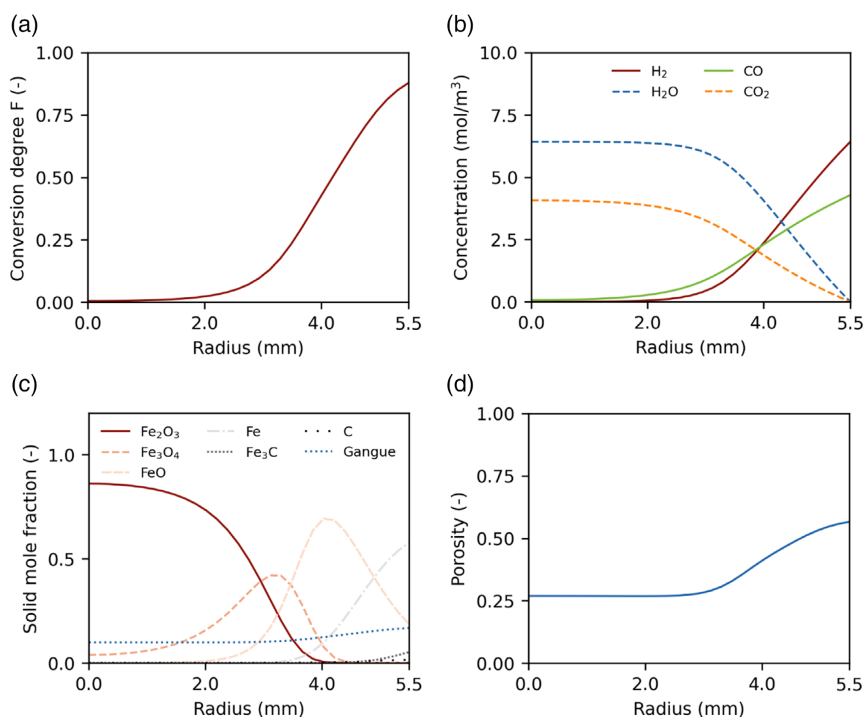

Figure 4. a) Local conversion degree, b) gas species concentration, c) solid mole fraction, and d) porosity. All four graphs are plotted versus the pellet radius. Data from 50% of reduction for Case 1 (see Figure 3).

Figure 5. a) Local conversion degree, b) gas species concentration, c) solid mole fraction, and d) porosity. All four graphs are plotted versus the pellet radius. Data from 50% of reduction for Case 2 (see Figure 3).
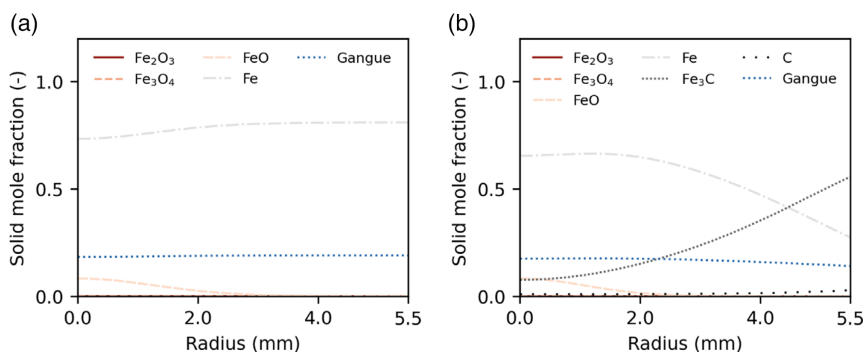

Figure 6. Solid mole fraction versus the pellet radius at the last time step of the simulation for a) Case 1 and b) Case 2.

near the pellet center. Some traces of FeO are visible near the core, the rest being Fe and gangue. In the syngas case, Figure 6b, an important part of the iron is in the carbide form. Free carbon is low in this case: the temperature is high and the gas is rich in hydrogen. The carbon does not accumulate excessively.

3.2. Results of the CFD Simulations

The previous section solved two reduction cases of single iron ore pellets using the 1D model. This led to the development of a set of chemical parameters. Now the same test cases will be simulated in the CFD environment. We will see that the CFD results can be used to derive boundary conditions and that ultimately both models can be coupled.

3.2.1. Numerical Setup

The numerical setup follows the experimental configuration described in Kazemi et al.[13] Pure hydrogen or syngas is injected from a tube having an inner diameter of 3 mm that conducts to the main reactor of 55 mm diameter. As the setup is fully axisymmetric, a 2D geometry was chosen. In total, the domain comprises 20 300 cells, of which 1464 belong to the pellet region. The cells in the pellet region and in the vicinity were refined in the two directions of interest.

3.2.2. Fields of the Reducing Agent

The direct use of these parameters in the CFD model will lead to deviations in the results, as in this modeling framework, the gas
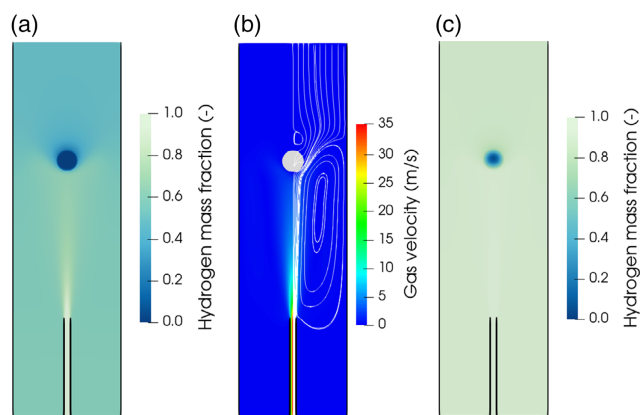
ADVANCED
SCIENCE NEWS
www.advancedsciencenews.com

steel
research
international

www.steel-research.de

Figure 7. Contour fields of the hydrogen case. a,c): hydrogen mass fraction at 20 and 600 s and b) gas velocity and streamlines.

region is also solved. This can be visualized in **Figure 7**. Figure 7a shows the hydrogen field after 20 s for the hydrogen case. The pellet region is filled with steam (H_2 concentration close to zero). Strong gradients of hydrogen can be observed in the vicinity of the pellet. There is also a strong asymmetry between the pellet upstream and downstream side. This is correlated with the gas phase velocity contour, Figure 7b, which shows how the bottom (upstream) side is subject to a much higher gas flow than the downstream part. At a later stage of the simulation, this external transport limitation becomes smaller. This can be seen in Figure 7c which depicts the same test case at 600 s. The hydrogen mass fraction is close to unity. This can be easily understood from the conversion degree over time. The rate of reduction (i.e., the slope of the curve) is highest at the beginning and continuously decreases. Therefore, with a constant mass flow rate of hydrogen injection, the external transport limitations are particularly important in the initial stage.

3.2.3. Coupling of the 1D and the CFD Models

The blue line in **Figure 8**a is the conversion degree over time for the first CFD simulation run. This curve lies clearly below the experimental values. This was expected because of the external transport limitations. In the next step, the information on the

boundary gained from the CFD simulations are incorporated into the 1D model to account for these limitations revealed in the CFD model. The hydrogen concentration at the pellet surface is not uniform because of the asymmetry discussed previously. Therefore, the average value over the surface was used to derive the hydrogen concentration profiles given in Figure 8b. The blue line corresponds to this first simulation run. Then, an iterative process takes place: new sets of chemical parameters for the three reactions with hydrogen are determined with the 1D model, then reused in the CFD simulations resulting in new boundary conditions. Convergence is reached after a few iterations, here 3, as depicted in Figure 8.

Once final values have been obtained for the reaction rates involving hydrogen, a similar iteration process is performed with Case 2, to obtain the other reaction rates. The final parameter set is given in **Table 3**.

The results with the final values are displayed in **Figure 9**. The CFD results are extremely close to the ones of the base model. Both models deliver the same results. Deviations are minimal and can be attributed to numerical residuals.

Further insight into the pellet region is given in **Figure 10**. All plots were taken from Case 2 at 50% of reduction. It is thus comparable to the results of the 1D previously presented in Figure 5. Figure 10a represents the CFD field of the pellet conversion degree. The asymmetry of the reduction inside the pellet appears clearly, with the bottom region showing a more advanced reduction stage. The profiles along the three lines represented in the CFD field are given in the same figure. We see that the

Table 3. Final set of chemical parameters obtained with resolved boundary conditions.

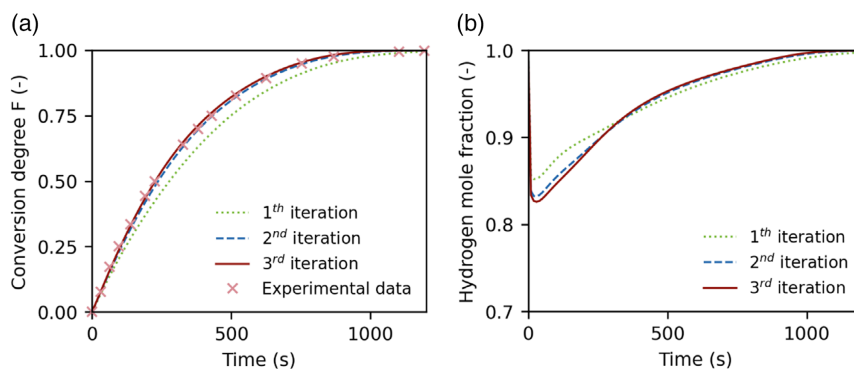| Reaction	Rate constant k
$3 Fe_2O_3 + H_2 \rightarrow 2 Fe_3O_4 + H_2O$	$61.7 \ s^{-1}$
$Fe_3O_4 + H_2 \rightarrow 3 FeO + H_2O$	$94.1 \ s^{-1}$
$FeO + H_2 \rightarrow Fe + H_2O$	$46.4 \ s^{-1}$
$3 Fe_2O_3 + CO \rightarrow 2 Fe_3O_4 + CO_2$	$20.8 \ s^{-1}$
$Fe_3O_4 + CO \rightarrow 3 FeO + CO_2$	$23.7 \ s^{-1}$
$FeO + CO \rightarrow Fe + CO_2$	$19.9 \ s^{-1}$
$2 CO \rightarrow C + CO_2$	$0.32 \ m^3 \ mol^{-1} \ s^{-1}$
$3 Fe + C \rightarrow Fe_3C$	$401 \ mol \ m^{-3} \ s^{-1}$

Figure 8. Case 1: a) Conversion degree over time for successive computational fluid dynamics (CFD) simulation runs and b) hydrogen mole fraction at the pellet surface over time derived from the CFD fields.
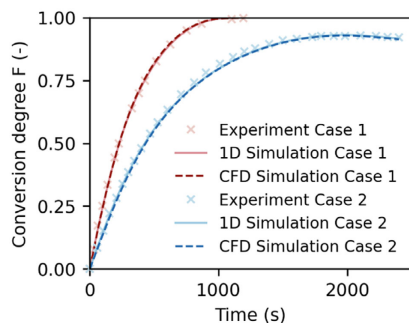
Figure 9. Conversion degree over time of the reduction of iron ore for Case 1 (in red) and Case 2 (in blue). The solid lines are the results of the 1D, and the dashed lines are the results of the CFD model.

horizontal and the top lines have very similar profiles; only the bottom line shows an important deviation. This region is flushed directly by fresh reducing gas, which explains the faster reduction. The red dashed line corresponds to the results of the 1D model. The shape also agrees very well with the CFD results and the value is between the bottom zone and the other regions.

The mole fractions of iron and all oxides are given in Figure 10b–d at the same simulation time. Here also, the relative asymmetry can be observed. The slowest process is the conversion of wüstite to iron; hematite and magnetite are at this stage only contained in the pellet core. The sum of the oxide mole fractions does not reach one because of the gangue content. The carbon content is low at this stage of reduction. The bottom region

shows higher carbon amounts, which can be explained by a more advanced stage within the reduction process.

The correct transport modeling is of great importance to achieve accurate and reliable heterogeneous chemistry models. If the transport limitations are not properly considered, the intrinsic chemistry cannot be obtained, and only apparent values are derived. As an example, the initial rates calculated for the reduction with hydrogen are a factor of two smaller than the final value. In the present cases, 2 and 1 L min^{-1} were introduced in the reactor for the hydrogen and the syngas cases, respectively. These values are high enough to limit the external transport limitations for one pellet. Still, the asymmetry is more critical in the syngas case and it can be expected that a value below 1 L min^{-1} would significantly amplify this phenomenon.

4. Conclusion

A porous solid model for the direct reduction of iron ore pellets has been presented. This model relies on a limited number of assumptions, the major ones being the consideration of the solid phase as ideal and the spherical symmetry assumption of the reduction process. The model solves for the individual species of the gas phase and the solid phase over the radius and the time. It was also demonstrated that the porosity equation can be solved for simultaneously with the species equations. This establishes the basis for a reliable description of the transport phenomena, and ultimately detailed kinetics can be developed. As an example, two test cases were considered, one involving pure hydrogen and the second a syngas.
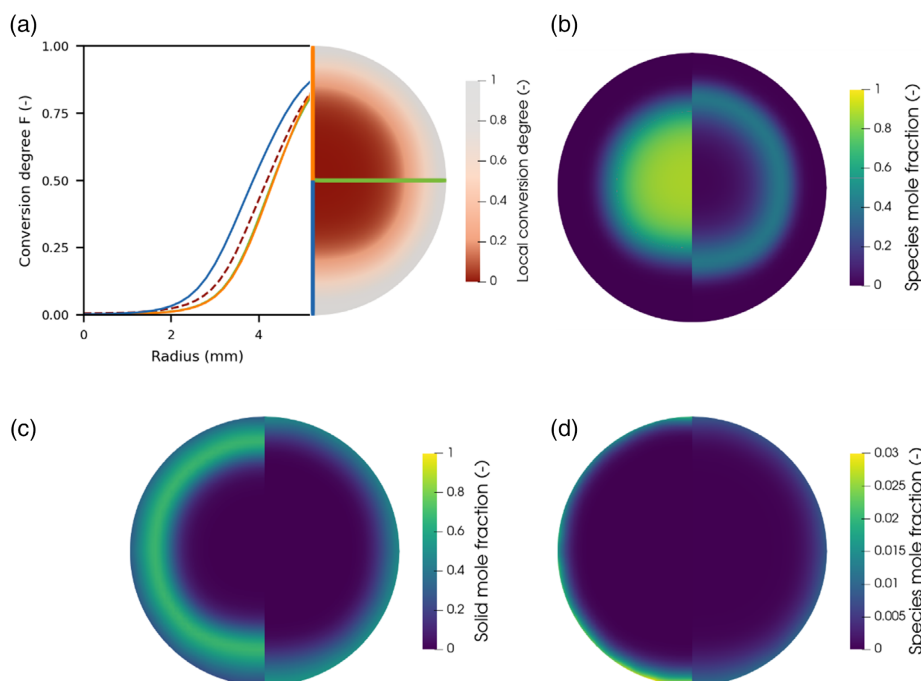

Figure 10. a) Contour plot of the local conversion degree at 430 s for Case 2 and associated profiles along the blue, green, and orange lines; the profile of the 1D model is also shown with the dashed red line. b–d) Contour plots of the solid species mole fractions. In order, b) left: Fe$_2$O$_3$, right: Fe$_3$O$_4$, c) left: FeO, right: Fe, and d) left: Fe$_3$C, right: C. Note that the scale in the last plot differs from the others for visibility.

The 1D model has later been integrated into a CFD environment. The whole reactor domain is considered and transport equations, valid inside the pellet and in the rest of the reactor, are solved. These two models have been interconnected. The former and faster model can determine physical parameters, like reaction rates. The second one solves, among others, the gas species concentration at the pellet surface and thus can deliver additional information for the 1D model. In this way, more accurate chemistry models can be obtained, as the transport limitations are considered. It was shown that the transition from the base model to the CFD model can be implemented consistently. All necessary governing equations and their sub-models were correctly integrated.

The present work allows further investigations, such as reducing iron ore pellets with syngas or methane, which involves homogeneous reactions, and also the transition to multi-pellet simulations with a high reliability.

Conflict of Interest

The authors declare no conflict of interest.

Data Availability Statement

The data that support the findings of this study are available from the corresponding author upon reasonable request.

[1] World Steel Association, *World Steel in Figures*, Brussels **2021**, https://worldsteel.org/steel-by-topic/statistics/world-steel-in-figures/.

[2] D. Rossetti di Valdalbero, N. Lucas, *European Steel The Wind Of Change: Energy In Future Steelmaking Steel In The Energy Market Applications Greening European Steel*, Publications Office of the European Union, Luxembourg **2018**.

[3] ESTEP AISBL, *Clean Steel Partnership Strategic Research and Innovation Agenda (SRIA)*, Brussels, October **2021**, https://www.estep.eu/library/publications/.

[4] T. Okosun, S. Nielson, C. Zhou, *JOM* **2022**, *74*, 1521.

[5] S. D. Angeli, S. Gossler, S. Lichtenberg, G. Kass, A. K. Agrawal, M. Valerius, K. P. Kinzel, O. Deutschmann, *Angew. Chem. Int. Ed.* **2021**, *60*, 11852.

[6] K. Rechberger, A. Spanlang, A. Sasiain Conde, H. Wolfmeir, C. Harris, *Steel Res. Int.* **2020**, *91*, 2000110.

[7] H. Hamadeh, O. Mirgaux, F. Patisson, *Materials* **2018**, *11*, 1865.

[8] A. Bonlade, A. Henriquez, M. Manrique, *ISIJ Int.* **2005**, *45*, 1255.

[9] R. Beheshti, J. Moosberg-Bustnes, R. E. Aune, in *TMS 2014: 143rd Annual Meeting & Exhibition ; Annual Meeting Supplemental Proc.*, Springer, Cham, Switzerland **2016**, pp. 495.

[10] E. Kawasaki, J. Sanscrainte, T. J. Walsh, *AIChE J.* **1962**, *8*, 48.

[11] M. Kazemi, *Effect Of Experimental Conditions On Cementite Formation During Reduction Of Iron Ore Pellets* KTH Royal Institute of Technology, Sweden **2016**.

[12] D. Guo, L. Zhu, S. Guo, B. Cui, S. Luo, M. Laghari, Z. Chen, C. Ma, Y. Zhou, J. Chen, B. Xiao, M. Hu, S. Luo, *Fuel Process. Technol.* **2016**, *148*, 276.

[13] M. Kazemi, B. Glaser, D. Sichen, *Steel Res. Int.* **2014**, *85*, 718.

[14] S. Geng, H. Zhang, W. Ding, Y. Yu, *Metalurgija* **2018**, *57*, 219.

[15] E. T. Turkdogan, J. V. Vinters, *Metall. Mater. Trans. B* **1971**, *2*, 3175.

[16] N. Towhidi, J. Szekely, *Metall. Mater. Trans. B* **1983**, *14*, 359.

[17] M. Kazemi, M. S. Pour, D. Sichen, *Metall. Materi. Trans. B* **2017**, *48*, 1114.

[18] M. S. Valipour, M. Y. Motamed Hashemi, Y. Saboohi, *Adv. Powder Technol.* **2006**, *17*, 277.

[19] E. Mousa, S. Ghali, Effect of H_2/CO Ratios on the Reduction Kinetics and Mechanism of Iron Ore Pellets, **2014**, http://steel-grips.com/articles/2014/sg14004.pdf.

[20] A. Z. Ghadi, M. S. Valipour, S. M. Vahedi, H. Y. Sohn, *Steel Res. Int.* **2020**, *91*, 1900270.

[21] A. Ajbar, K. Alhumaizi, M. Soliman, *Ironmak. Steelmak.* **2011**, *38*, 401.

[22] A. Mirzajani, H. A. Ebrahim, S. Nouri, *Braz. J. Chem. Eng.* **2018**, *35*, 1019.

[23] D. G. Goodwin, R. L. Speth, H. K. Moffat, B. W. Weber, Cantera: An Object-Oriented Software Toolkit for Chemical Kinetics, Thermodynamics, And Transport Processes, Version 2.5.1 **2021**, https://www.cantera.org, 2021.

[24] J. B. Butt, *Reaction Kinetics And Reactor Design*, CRC Press, Boca Raton, FL **2000**.

[25] S. Hamdi, W. Schiesser, G. Griffiths, *Scholarpedia* **2009**, *2*, 2859.

[26] A. N. F. Versypt, R. D. Braatz, *Comp. Chem. Eng.* **2014**, *71*, 241.

[27] OpenFOAM, https://openfoam.org/, (accessed: January 2022).